ELSEVIER

Materials Science and Engineering A257 (1998) 256–267

MATERIALS SCIENCE & ENGINEERING A

The strain rate and temperature dependence of the dynamic impact response of tungsten composite

Woei-Shyan Lee *, Guo-Liang Xiea, Chi-Feng Lin

Department of Mechanical Engineering, National Cheng Kung University, Tainan 70101, Taiwan, ROC

Received 22 June 1998; received in revised form 27 July 1998

Abstract

Liquid sintered tungsten (W) heavy alloy with a 92.5W–5.25Ni–2.25Fe composition was examined using a compression split-Hopkinson bar to realize the effects of strain rate and temperature on dynamic impact deformation behaviour. Both stress and strain were measured for specimens tested at temperatures ranging from 25 to 1100°C and strain rates ranging from 8×10^2 to 4×10^3 s^{-1}. The relationship between flow stress, strain rate and temperature was determined and the results have been successfully modeled by a proposed constitutive equation incorporating the effect of strain, strain rate and temperature. Our results show that flow stress increases with increasing strain rate. Alternatively, high temperature reduces flow stress significantly and improves the degree of thermal softening. During impact, initial cracking occurs preferentially either at tungsten–tungsten grain boundaries or at the tungsten–matrix interface, and failure is dominated principally by a mixture fracture model. Metallographic examinations show a dramatic increase in microcrack density and deformation of tungsten grains as strain rate and temperature are increased. Additionally, changes in microhardness are also found to correlate with changes in strain rate and temperature. © 1998 Elsevier Science S.A. All rights reserved.

Keywords: Compression split-Hopkinson bar; Dynamic fracture; Microcrack density; Strain rate and temperature sensitivities; Tungsten composite; Tungsten grain deformation

1. Introduction

Tungsten (W) heavy alloy is a particle composite which contains a very large percentage of nearly spherical tungsten particles embedded in a ductile matrix of nickel–iron. This composite structure results in a high density material with a useful combination of mechanical properties: high strength, moderate ductility and outstanding thermal conductivity. These properties make this class of materials an attractive candidate for many military and civil applications [1,2]. Therefore, there have been a large number of reports on the effect of composition, interphase interface structure, sintering conditions and thermomechanical processing on the material's mechanical properties [3–9]. However, the most demanding uses of tungsten composite are dependent on the material's high strain rate properties, especially for penetrator applications. From the structural design point of view, the high strain rate and high temperature strength of tungsten composite appear of particular importance in obtaining the best penetration behaviour of armor-piercing projectiles and the best fabrication behaviour from the warm swaging process. It seems desirable, then, to study composite tungsten's dynamic impact response in terms of microstructural variations caused by large strains developed at both high rates and high temperatures.

It is probable that plastic deformation behaviour and the fracture mode of tungsten composite under impact loading are significantly complex and may be assumed to depend on a rather complicated combination of deformation rate, loading temperature, tungsten grain volume fraction and the composition of the interface matrix [10–14]. Several studies have attempted to correlate observed mechanical properties with these deformation variables and microstructural parameters. For example, Woodward et al. [15] reported room temperature strain rate effects on the compression flow stress of three heavy tungsten alloys. Their results showed that

* Corresponding author. Tel.: +886 6 2757575; fax: +886 6 2352973.

0921-5093/98/$ - see front matter © 1998 Elsevier Science S.A. All rights reserved.
PII S0921-5093(98)00852-1

softening often occurs at the higher strain rates, which can be attributed to cracking and self-heating of the specimens. Lee and Chiou [16] recently presented results for low and high rate shear deformation behaviour of tungsten composites at room temperature. Their results indicated that a strong increase in strain rate sensitivity is observed at strain rates exceeding 10^3 s^{-1}, and that grain deformation and microcrack density depend strongly on strain rate levels. In terms of the effects of test temperature, various studies have reported that a major ductility loss occurs at temperatures below 100°C [14,17–19]. O'Donnell and Woodward [20] tested a tungsten alloy and found that, in the range of -100 to 300°C, under strain rates of 2×10^{-4} and 7 s^{-1} for both tension and torsion tests, a decrease in temperature resulted in an increase in flow stress. German et al. [21] presented the variation of toughness with test temperature and cooling rate for a two-phase heavy alloy composite at temperatures of -100, 22 and 300°C, and suggested different fracture path possibilities in the liquid phase sintered alloy.

On the basis of these previous investigations, it is clear that the effects of strain rate and temperature are substantial in the deformation and fracture behaviour of tungsten composite. However, systematic studies combining high strain rate and high temperature effects for tungsten composites are few, leaving unclear many aspects of the composite's deformation, strain hardening and rate mechanisms under high temperature conditions. Thus, this paper focuses particularly on the dynamic impact response of tungsten composite in the temperature range of 25–1100°C, thereby allowing evaluation of the influence of high rate and high temperature on the composite's impact properties and fracture characteristics and filling a gap in the literature data for the elevated temperature range.

2. Experimental procedure

2.1. Material and specimen preparation

A 92.5W–5.25Ni–2.25Fe (weight percentages) heavy alloy fabricated by liquid-phase sintering of the blended elemental powders was used in this study. The material has a density of 17.5 g cm^{-3}, a total impurity content of less than 450 ppm by weight, and mean tungsten grain size of 24 ± 9 μm. Fig. 1 presents a typical microstructure of this tungsten composite, showing a section perpendicular to the axis of the swaged rod. The microstructure consists of spherical b.c.c. grains of almost pure tungsten embedded within an f.c.c. W–Ni–Fe matrix. The specimens, having a simple right-cylindrical geometry 10 mm in diameter and 5 mm in height, were cut from a sintered bar of 12 mm diameter in such a way that the compression axis was along the swaged direction. The surface of the two end faces were parallel within 0.05 mm. After polishing the specimens down with 1200 grit emery paper, the surface of each end was lubricated with two different kinds of lubricant: molybdenum disulfide (molykote) was used for lubrication at temperatures below 300°C, and glass paste was used in the higher temperature range of 500–1100°C.

2.2. Experimental techniques

Mechanical testing was performed using a split-Hopkinson bar at strain rates ranging from 8×10^2 to 4×10^3 s^{-1} and at temperatures of 25, 300, 500, 700, 900 and 1100°C. Fig. 2 shows a schematic drawing of the test set-up used in this study. This apparatus consisted of incident and transmitter pressure bars on which SR-4 gages monitored the incident and transmitted pulses. The projectile, incident bar and transmitter bar were made from DC53 die steel with a diameter of 12.5 mm. The length of the incident and transmitted pressure bars was 1 m, while the striker bar was 317 mm. Some mechanical characteristics of the DC53 die steel bar are presented in Table 1. The lubricated specimen was mounted between the incident and transmitted bars, and impact was provided by a striker bar propelled by a horizontal pressure system acting as a gun to fire the striker bar. To ensure the occurrence of fracture in the material by the first pulse during compression testing, an interrupting collar was placed around the specimen. For temperature tests, the specimen was heated by an in situ induction coil with a ceramic tube, and the temperature was regulated to an accuracy of ± 2°C by a Eurotherm 211 programmer/controller connected to a Inconel sheathed chromel–alumel thermocouple, 1.5 mm in diameter, placed as close as possible to the surface of the specimen. The measurement of temperature distribution shows that the temperature, at 40 cm from the center is only

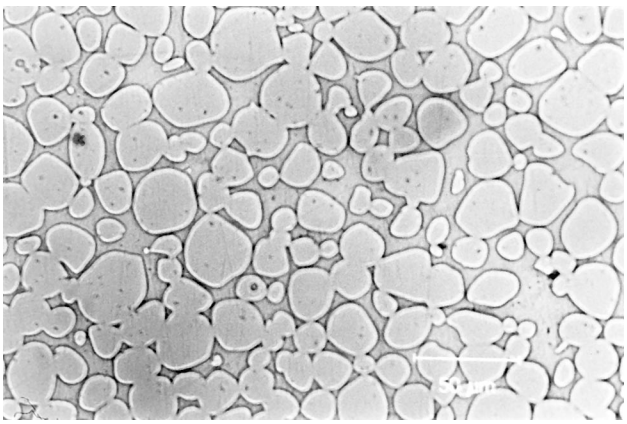

Fig. 1. Microstructure of the W–Ni–Fe composite, containing (wt.%) 92.25W, 5.25Ni and 2.25Fe.

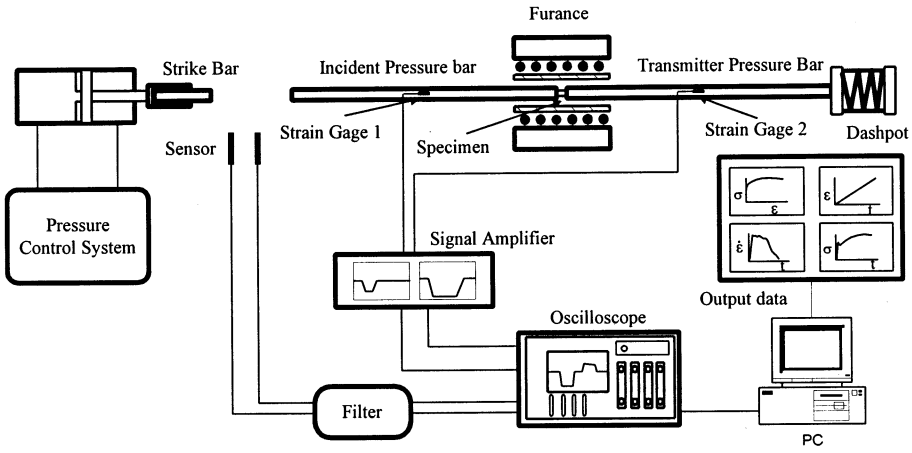

Fig. 2. Schematic presentation of the compression split-Hopkinson bar apparatus.

slightly above room temperature and therefore has a neglible effect on the nearest strain gage at 50 cm from the center, as shown in Fig. 3.

During dynamic testing, the passage of the pulse was measured by strain gages placed on the incident and transmitted bars. Strain gage 1 (Fig. 2) recorded the incident pulse (ϵ_I), while strain gage 2 recorded the transmitted pulse (ϵ_t). Based on one-dimensional elastic wave propagation theory and on the records of incident, reflected and transmitted pulses (ϵ_I, ϵ_r, ϵ_t), the average compression strain ϵ, strain rate $\dot{\epsilon}$ and stress σ in the specimen can be obtained by:

$$\epsilon_s = \frac{-2C_0}{L_0}\int_0^t \epsilon_r dt \quad (1)$$

$$\dot{\epsilon}_s = \frac{-2C_0}{L_0}\epsilon_r \quad (2)$$

$$\sigma = \frac{EA}{A_0}\epsilon_t \quad (3)$$

where C_0 is the longitudinal wave velocity in the split-Hopkinson bar, L_0 the effective gage length of the specimen, E the Young's modulus of the split bar, while A and A_0 are the cross-sectional areas of the split bar and the specimen, respectively.

It should be noted that, for those tests performed at temperatures higher than 300°C, especially near the upper end of our temperature range, because the ends of the pressure bar extend into the furnace and are also heated, there is a thermal gradient distributed along the bars as shown in Fig. 3. Thus, Eqs. (1)–(3) for determining the strain, strain rate and stress of specimen under room temperature condition must be modified. By considering the effect of the thermal gradient on the bars, specimen strain is calculated by:

$$\epsilon_s = \left(\frac{2C_\alpha}{L_0}\right)\int_0^t (\epsilon_{I\alpha} - \epsilon_{T\beta} - \epsilon'_\alpha)\, dt \quad (4)$$

where $\epsilon_{I\alpha}$ and $\epsilon_{T\beta}$ are obtained from strain pulses ϵ_I and ϵ_T, which are recorded at the incident and transmitter bar gage stations but corrected in amplitude according to the following relations. These relations compensate for pulse changes caused by transmission through the thermal gradient:

$$\frac{\epsilon_T}{\epsilon_I} = \frac{2E_1}{(E_2 + E_1E_2)^{1/2}} \quad (5)$$

where E_1 and E_2 are the modulii of elasticity on the two sides of the thermal gradient area of the bars and are dependent of temperature. ϵ'_α is a reflection pulse which can be determined from $\epsilon_{I\alpha}$ and $\epsilon_{T\beta}$. Eq. (4) is used to calculate specimen strain in the high temperature ranges. The time in Eq. (4) is measured at the instant that the incident strain pulse reaches the specimen. It can be seen that to determine the specimen strain does not require a record of the reflected pulse at the incident gage station.

The stress in the specimen is obtained from the strain at the face of the transmitter bar in contact with the specimen, i.e. $\epsilon_{T\beta} + \epsilon'_\beta$. Since this bar remains elastic, we have:

$$\sigma_s = E_p(\epsilon_{T\beta} + \epsilon'_\beta) \quad (6)$$

where ϵ'_β is a pulse that can be determined from $\epsilon_{I\alpha}$ and $\epsilon_{T\beta}$. This high temperature testing technique has been described in detail in our earlier investigation [22].

Table 1
Some mechanical characteristics of DC53 die steel bars

Density (ρ)	7.87 g cm^{-3}
Young's modulus (E)	212.8 GPa
Shear modulus (G)	83.16 GPa
Poisson's ratio (ν)	0.28
Wave velocity (C_0)	5200 m s^{-1}
Yield stress (σ_y)	2880 MPa

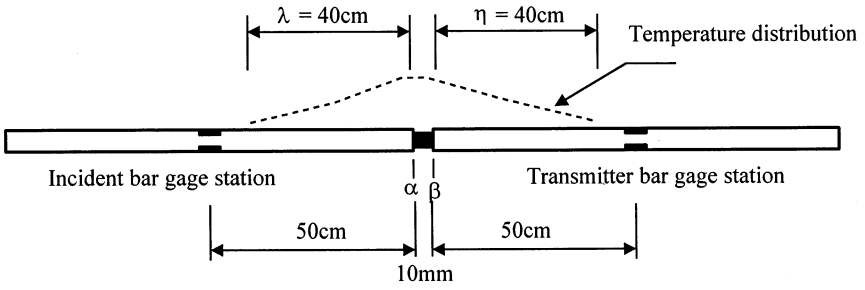

Fig. 3. Temperature distribution and strain gage stations of bars.

2.3. Metallography

After impact testing, metallographic examinations were conducted of the variations of tungsten grain deformation and microcrack density as well as the changes of fracture characteristics in terms of tested temperature and strain rates. For optical metallographic observations, deformed specimens were mounted and polished with diamond paste of a mean particle size of 1.0 μm; final polishing was performed with 0.05-μm alumina. The specimens were then observed with an MeF3 optical microscope. The changes in degree of tungsten particle deformation were determined using a shape factor K_2 based on the relation between the longest and shortest particle diameter. Microcrack densities were measured by linear analysis of optical photographs (magnification 220 ×). At least ten measurements were taken on the observation surface of each specimen. Microhardness measurements were performed on individual tungsten grains and matrix regions by means of a Matsuzawa MXT 70 microhardness tester with a load of 25 g. Ten Vickers indentations were made per phase in each of the deformed specimens. The reported hardness values are averages of these ten readings. Fractured specimens were examined by a JXA-840 scanning electron microscope operating at an acceleration potential of 20 kV.

3. Results and discussion

3.1. Flow stress–strain behaviour

Typical flow stress–strain curves for the W–Ni–Fe composite deformed at different strain rates are shown in Fig. 4(a)–(d). For each strain rate, the temperature was varied from 25°C up to 1100°C, except for the strain rate of 8×10^2 s^{-1} (Fig. 4(a)), where the tests were performed at temperatures ranging from 25 to 700°C. In comparing these curves, it is evident that the flow stress–strain behaviour of the W–Ni–Fe composite is fairly sensitive to the strain rate and temperature. As deformation occurs at constant temperature under a fixed strain, the flow stress increases with an increase of strain rate. However, at any specific strain rate, an increase of temperature results in a decrease of flow stress. Another interesting observation that can be made from Fig. 4(d) is that, at the highest tested strain rate, 4×10^3 s^{-1}, the flow stress increases with strain up to a true strain of 0.2, then decreases considerably with increasing true strain for all temperatures. This decrease in flow stress may be attributed to two factors. First, under very high deformation rates and high strain values, the rate of thermal softening is greater than that of work hardening, because, during deformation, the plastic work done may be converted to heat, which produces a rise of temperature in the specimen. The second factor that may lead to a drastic reduction in the flow stress is the formation and coalescence of microcracks in the internal structure. In fact, as presented in Fig. 4(d), the point of maximum stress is important inasmuch as it represents the strain at which damage of the material begins to occur. This phenomenon can also be verified from our microstructural observations.

3.2. Strain rate effect

The stress–strain curves plotted in Fig. 4(a)–(d) show an obvious effect of strain rate on flow stress for all testing temperatures. This strain rate effect can be more clearly seen by plotting flow stress as a function of logarithmic strain rate. Fig. 5(a) Fig. 5(b) represent the relationship between flow stress and the logarithm of strain rate for constant plastic strains of 10% and 20%, respectively, at various temperatures. As may be seen, flow stress increases with strain rate for all testing temperatures, with an approximately linear relationship. This linear dependence has been obtained by a number of investigators for many other materials [23–25]. It is important to note that as the strain rate goes higher than 2.5×10^3 s^{-1} and the deformation progresses above 20%, as shown in Fig. 5(b), there is an abrupt change in strain rate sensitivity from positive to negative due to thermal softening and internal structural damage. This strong dependence of flow stress on the logarithm of strain rate and temperature suggests that the deformation mechanism associated with high

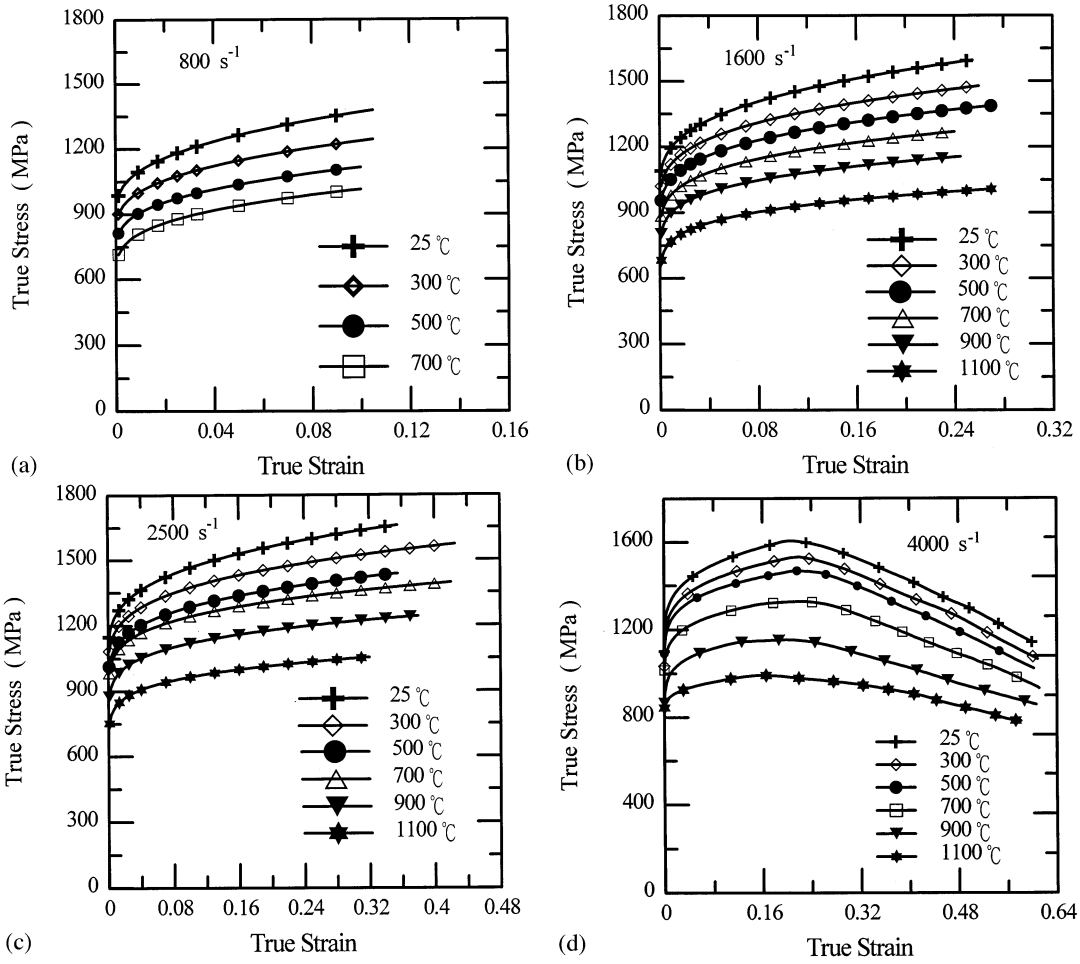

Fig. 4. Temperature dependence of true stress–strain curves compression at: (a) 8×10^2 s^{-1}; (b) 1.6×10^3 s^{-1}; (c) 2.5×10^3 s^{-1}; (d) 4×10^3 s^{-1}.

rate compression loading is a thermally activated process. A deformation of this type can be described by the Arrhenius rate controlling equation, $\dot{\epsilon}_p = \epsilon_0 \exp(-\Delta G_{\tau^*,T}/KT)$, and the total applied stress can be divided into two components: an athermal component and a thermally activated component. The former is influenced only by the material's structure, while the latter depends extensively upon the temperature and strain rate.

3.3. Temperature effect

As mentioned previously, test temperature has a very strong effect on flow stress, particularly in the high temperature regime: the higher the temperature, the lower the flow stress. In order to better represent quantitatively this dependence, a temperature sensitivity is introduced and expressed as:

$$n_a = \frac{\ln(\sigma_2/\sigma_1)}{\ln(T_2/T_1)} \quad (7)$$

where $T_2 > T_1$, and $T_1 = 25$°C. Using this definition and the data depicted in Fig. 4(a)–(d), the value of temperature sensitivity is calculated over the tested range of strain rates and temperatures. Fig. 6 shows the relationship between the temperature sensitivity, n_a, with true strain for specimens deformed at 1.6×103 s^{-1} under different temperature ranges. As can be seen, an increase in true strain results in a slight increase in temperature sensitivity for each temperature range. However, at a fixed true strain, the temperature sensitivity increases rapidly with temperature increment. The effect of true strain on temperature sensitivity compared with the effect of temperature increment on temperature sensitivity shows that the degree of thermal softening caused by the temperature increment is distinctly greater than that caused by straining. The results also indicate that, under high rate and high temperature loading, deformation behaviour is dominated by the thermal softening process, which represents the effect of thermal activation overcoming dislocation flow barriers as the temperature is raised.

Since temperature sensitivity is relatively independent of true strain levels, for comparison purposes, we can neglect the effect of plastic strain and take an average temperature sensitivity value for each temperature

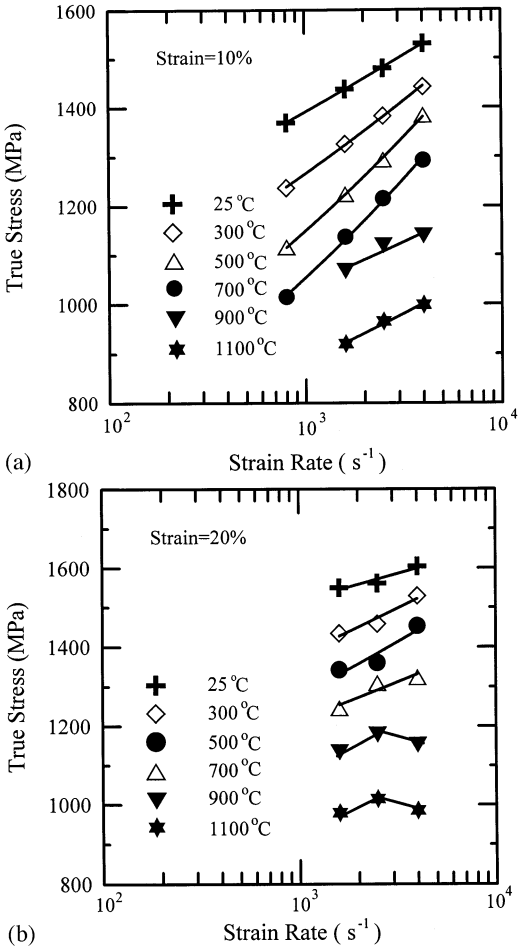

Fig. 5. Influence of strain rate on flow stress at a constant plastic strain of (a) 10% and (b) 20%, as a function of temperature.

range under different strain rate conditions. The plot of Fig. 7 shows the variation of average temperature sensitivity with temperature for four tested strain rates.

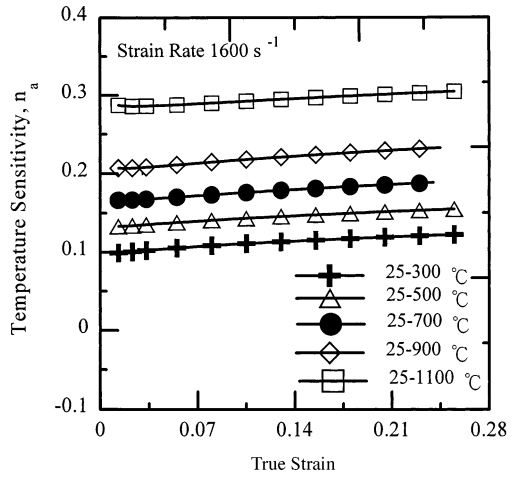

Fig. 6. Variation of temperature sensitivity as a function of plastic strain for a strain rate of 2.5×10^3 s^{-1} under different temperature ranges.

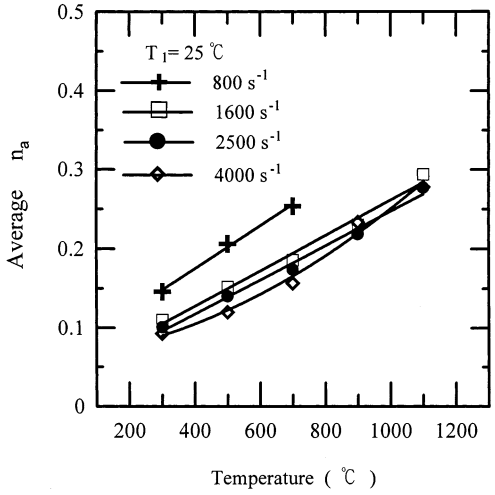

Fig. 7. Variation of temperature sensitivity as a function of temperature under different strain rates.

The average temperature sensitivity is also temperature dependent. It increases with temperature for each strain rate, but decreases with increasing strain rate for a given temperature. This can be explained as a competition process between the rate of work hardening caused by high rate plastic deformation and the rate of thermal softening resulting from the rise of temperature. Obviously, the rate of thermal softening dominates the rate of work hardening in controlling flow resistance behaviour and thus plays the leading role in the temperature sensitivity characteristics. Therefore, in order to describe flow stress as a function of strain, strain rate and temperature, thermal softening which results from thermally activated processes should be taken into consideration when rationalizing the flow behaviour. This can be done expressing the flow stress as a function of dislocation density and the rate of dislocation annihilation.

3.4. Deformation constitutive equation

As pointed out in Section 3.1, the plastic deformation characteristics of W–Ni–Fe composite are strongly dependent on strain, strain rate and temperature. Because the influences of these three factors are independent of each other, it is important to combine the effect of these variables in a constitutive equation that can be used in computer code to model the deformation response of this material for high rate and high temperature conditions. There are currently many different constitutive models available that describe the behaviour of specific materials [26–29]. In this study, a dislocation mechanics-based model for rate-dependent behaviour, proposed by Zerilli and Armstrong [29], is used to describe observed dynamic flow behaviour. This model is attractive because it distinguishes between the response of b.c.c. and f.c.c. metals. For the b.c.c. case, the model is represented by the following relation:

Table 2
Temperature increase values (ΔT) for specimens deformed at a strain rate of 2.5×10^3 s^{-1} and strains (ϵ) ranging from 0.05 to 0.3 under six initial test temperatures

Initial temperature tested (°C)	ΔT (°C)					
	$\epsilon = 0.05$	$\epsilon = 0.1$	$\epsilon = 0.15$	$\epsilon = 0.2$	$\epsilon = 0.25$	$\epsilon = 0.3$
25	20.892	44.137	68.441	93.53	119.26	145.53
300	19.695	41.529	64.295	87.744	111.75	136.22
500	18.467	38.909	60.193	82.087	104.47	127.27
700	17.933	37.716	58.254	79.333	100.84	122.21
900	16.153	33.979	52.513	71.503	90.869	110.55
1100	13.93	29.321	45.284	61.649	78.33	95.273

$$\sigma = C_0 + C_1[\exp(-C_3T + C_4T \ln \dot{\epsilon})] + C_5\epsilon^n \quad (8)$$

where C_0, C_1, C_3, C_4, C_5 and n are the parameters determined by the regression analysis procedure, $\dot{\epsilon}$ is the imposed strain rate, T is the test temperature, σ is stress and ϵ is strain.

The data in the plots of Fig. 4 is used to determine the coefficients and exponents of the constitutive equation by a regression analysis technique. Ideally, these parameters must be obtained from the stress–strain curves obtained in constant strain rate and constant temperature tests. However, during high strain rate deformation, because there is simply not enough time to conduct away the heat generated by the plastic work, it is impossible to keep the specimen under isothermal conditions. Thus the temperature rise in the specimen must be reckoned and a current temperature used to calculate flow stress in our simulation. Since a specimen's temperature rise is difficult to measure explicitly during high velocity impact, the magnitude of temperature rise is instead calculated by an integral equation:

$$\Delta T = \left(\frac{1}{\rho C_p}\right)\int_0^{\epsilon} \sigma \, d\epsilon$$

where ΔT is the temperature rise, ρ is the density (19.3 g cm^{-3}), C_p is the heat capacity (0.038 cal g^{-1} per °C), σ is the stress and $d\epsilon$ is the interval of strain. This calculation has been made for each of the tested temperature–strain rate conditions. Table 2 lists the increase in values of the temperature for specimens deformed at a strain rate of 2.5×10^3 s^{-1} and strains from 0.05 to 0.3 under six initial tested temperatures. Assuming that the form of the Zerilli–Armstrong model remains valid for our composite (which contains 92.5W) and replacing the initial temperature with the current temperature for each interval of strain in the regression process, we obtain best-fit parameters for describing our experimental results on the W–Ni–Fe composite (assuming that $C_0 = 0$) as follows: $C_1 =$ 1286.9 MPa, $C_3 = 1.9 \times 10^{-4}$, $C_5 = 825.5$ MPa and $n =$ 0.287. An example of the comparison between the predictions of the proposed model and experimental results are shown in Fig. 8, which corresponds to a strain rate of 1.6×10^3 s^{-1}. The agreement between the measured and predicted curves is good for each testing temperature, with a maximum error of 5%, which is sufficient for engineering purposes.

3.5. Fracture feature observations

The fracture features of deformed specimens were examined using optical and scanning electron microscopy. Our observations found that catastrophic failure at strain rates above 4×10^3 s^{-1}, for all tested temperatures, occurs by the mechanism of matrix microcrack formation associated with transgranular cleavage of tungsten grains. In general, the nickel–iron matrix fails predominantly in a ductile manner, while in the tungsten grains, brittle cleavage features are observed. Fig. 9(a) shows a fracture surface example obtained from a specimen deformed at 900°C and a strain rate of 4×10^3 s^{-1}. There are four possible fracture paths: tungsten–tungsten grain boundary separation, tungsten–matrix interfacial separation, tungsten

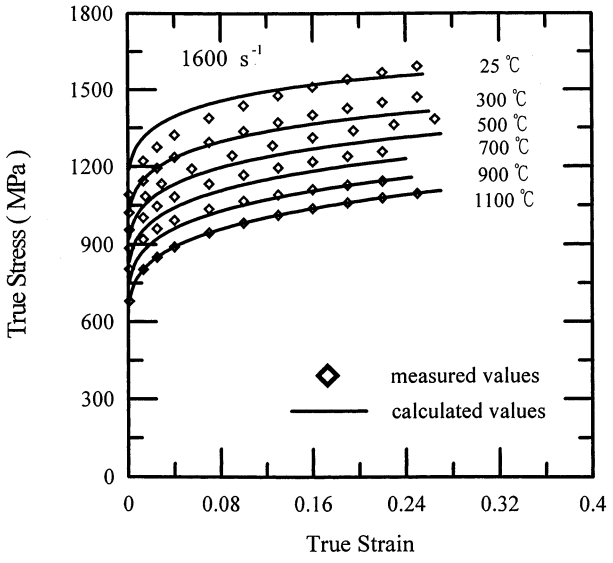

Fig. 8. Comparison between predicted and measured stress–strain curves for a strain rate of 1.6×10^3 s^{-1}.

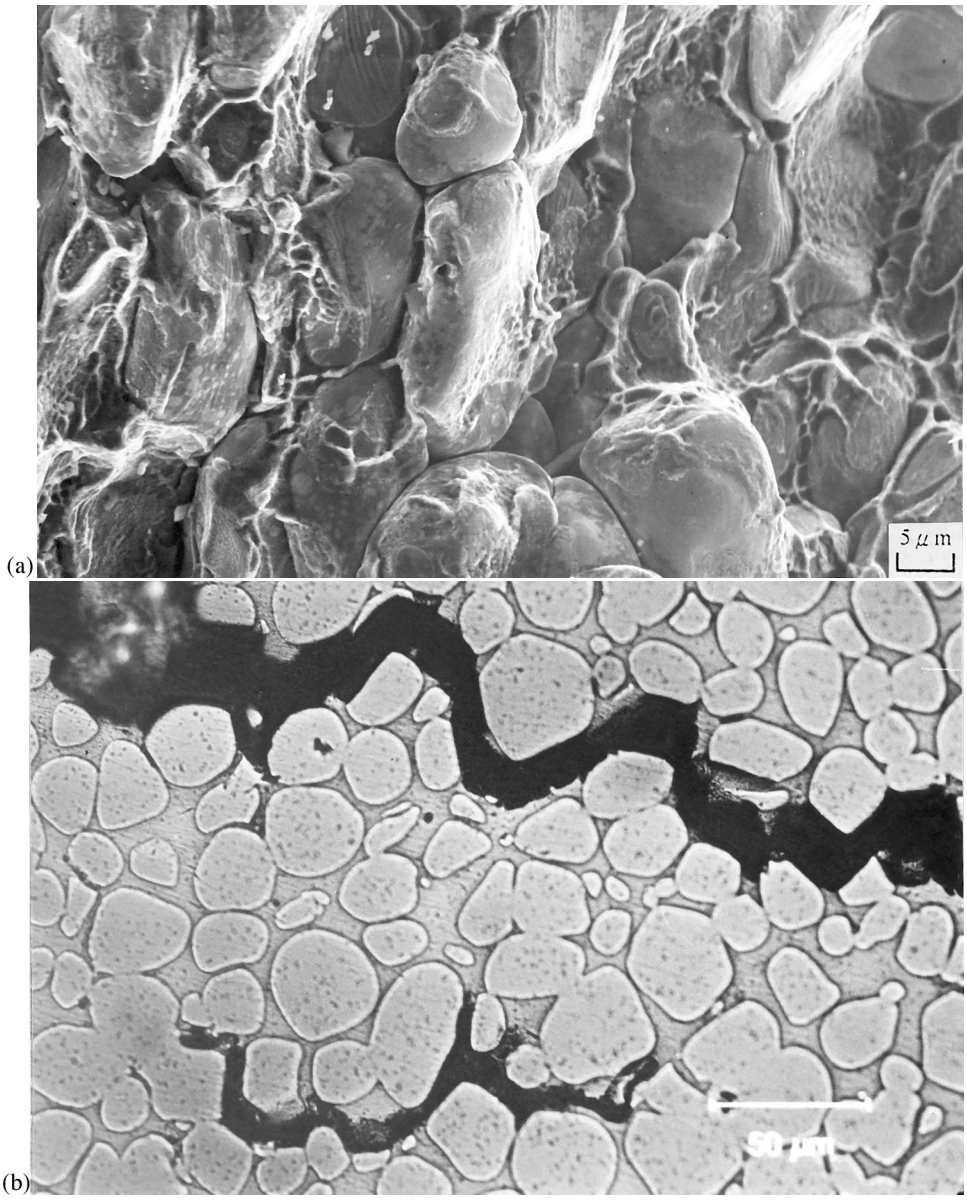

Fig. 9. Fracture features of specimens deformed at (a) 900°C (scanning electron micrograph) and (b) 25°C (optical micrograph) under a constant strain rate of 4×10^3 s^{-1}.

cleavage and matrix rupture. All four of these features can be observed on the fracture surface in all of our samples. If we focus on the fracture aspects of the Fe–Ni matrix, it appears that the matrix surface is characterized either by ductile shearing and localized tapering of the matrix as it is 'pulled out' from between tungsten particles, or by a dimpled appearance as the matrix fails by a form of void coalescence. By contrast, the tungsten grains fail predominately by transgranular cleavage, and a flat facet can be seen in the surface. These flat areas are frequently the result of cleavage of localized groups of tungsten grains.

Cracking of the tungsten grain by cleavage needs good transmission of stresses from the matrix to the spherical or ellipsoidal grains through the interface. If the matrix phase has a high strength associated with good ductility, during high rate deformation, a significant amount of applied stress will be induced and contributed to the deformation of tungsten grains. Therefore the enhancement of stress due to strain rate increase can lead to a rapid increase of transgranular fragmentation of tungsten grains. The fracture characteristics of the W–Ni–Fe composite can also be observed by optical micrographs taken from the specimen section perpendicular to the impact direction, as shown in Fig. 9(b), which corresponds to a specimen deformed at 25°C at 4×10^3 s^{-1}. In this instance, fracture occurs mainly by macrocracks propagating within the Fe–Ni matrix, microcracks at the interface between tungsten grains and matrix and, finally, microcrack formation

between contiguous tungsten grains. The combination of fracture features seen in Fig. 9(b) provides a good example for our explanation for the drop of flow stress observed in the stress–strain curves presented in Fig. 4(d). To the left of the true stress maximum in this figure, one finds few cracks of any sort in specimens. To the right, the cracking behaviour increases dramatically, leaving little doubt that the magnitude of flow stress drop follows the density of micro- and macrocracks.

3.6. Measurement of tungsten grain deformation and microcrack density

To measure the deformation of tungsten grains as a function of strain rate and temperature, photomicrographs were digitized by scanner and loaded into a PC. The shapes of 150–200 tungsten grains per sample were used for image analysis. Different methods were tested for transforming the shapes of the particles to a value representing the degree of average plastic deformation. The best result obtained in this study was found using a shape factor $K_2 = 4\pi A/U^2$, where A represents the area in mm^2 and U the circumference of the grain section. This shape factor is normalized in a way that the shape factor value of an undeformed grain is $K_2 = 1$, corresponding to 0% strain; 100% strain results in a shape factor of $K_2 = 0$. Using this technique, the deformations of tungsten grains were measured and are shown in Fig. 10. As expected, grain deformation depends strongly on the strain rate and temperature. An increase in both strain rate and temperature resulted in a marked increase in tungsten grain deformation. In the case of extremely dynamic plastic deformation (i.e. strain rate of 4×10^3 s^{-1} and temperature of 1100°C), a maximum deformation of 73% is observed. Although grain deformation correlates directly with strain rate

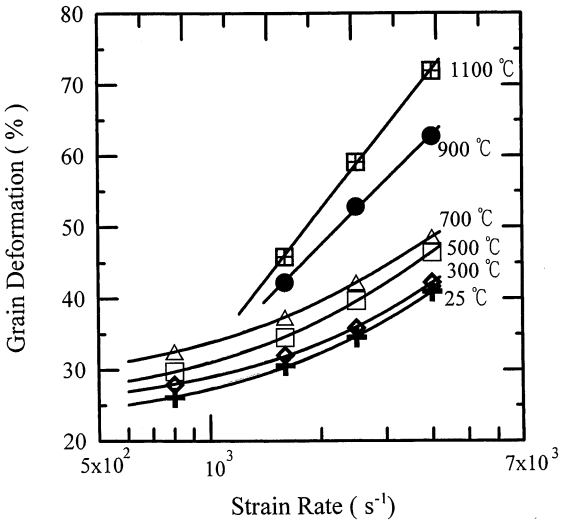

Fig. 10. Variation of tungsten grain deformation as a function of strain rate and temperature.

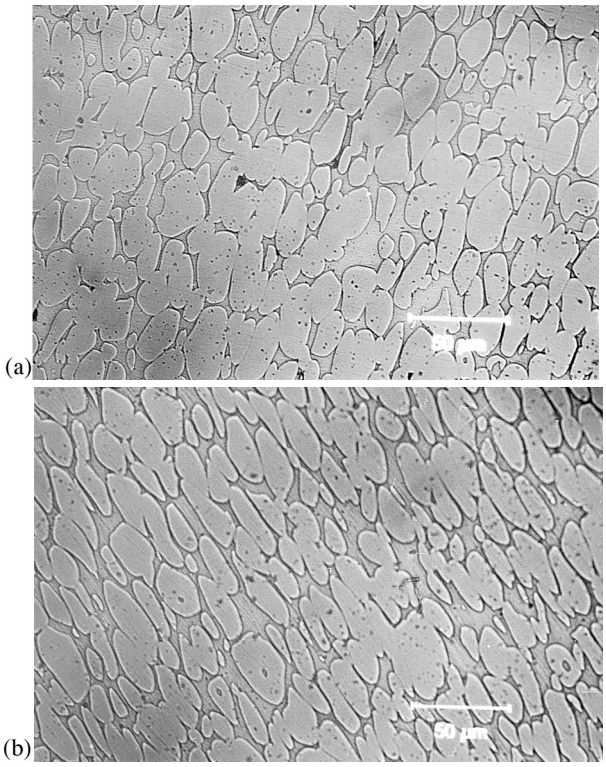

Fig. 11. Optical micrographs taken from the specimens deformed at (a) 300°C and (b) 1100°C under a fixed strain rate of 4×10^3 s^{-1}.

for each tested temperature, the slope of the curve is steeper as the temperature rises above 900°C. This means that deformation hardening of tungsten grains at very high temperatures is less than that obtained at temperatures below 700°C. Optical micrographic aspects of grain deformation taken from specimens deformed at 300 and 1100°C under a fixed strain rate of 4×10^3 s^{-1} are shown in Fig. 11(a)Fig. 11(b), respectively. Comparison of these two figures shows clearly an increase in tungsten grain deformation as temperature is increased. After heavy deformation, the shape of tungsten grains becomes an elongated ellipse all oriented in the same direction.

After carefully choosing the location of the indentation, in order to avoid interference from boundaries, the results from the microhardness tests for matrix and tungsten grain are shown in Fig. 12(a)Fig. 12(b), respectively. It is clear that the microhardness in both matrix and tungsten grain increases with increasing strain rate for all the temperatures. With regard to the temperature effect on the variation of microhardness, it is found that, at a fixed strain rate, the matrix microhardness decreases systematically as the temperature increases. A similar tendency can also be found in the tungsten grains, but there seems to be a scatter in the tungsten grain microhardness measurement (Fig. 12(b)) due to the effect of grain orientation. It has been reported that the rate of work hardening is very depen-

dent on the orientation of the load relative to the crystal orientation. This anisotropic hardening may be the cause of some of the scatter in the hardness measurements of the randomly oriented single-crystal tungsten grains found in the heavy alloy. Moreover, the data presented in Fig. 12(a)Fig. 12(b) indicate a greater degree of work hardening of the matrix in comparison with that of the tungsten grains during deformation occurring under our present test conditions.

Fig. 13 plots the microcrack density against the tested strain rate as a function of temperature, in which the influences of strain rate and temperature are obvious. For all temperatures, a significant augmentation in the microcrack density as a result of strain rate is observed. Moreover, at a given strain rate, the microcrack density seems to be greater for higher temperatures. Microstructural examinations of sectioned specimens reveal that initial cracking occurs preferentially either at tungsten–tungsten grain boundaries or at the tungsten–matrix interface. These can be seen in Fig. 14(a) and 14(b), which correspond to strain rates of 8×10^2 s^{-1} and 2.5×10^3 s^{-1}, at temperatures of 25 and 1100°C, respectively. Since liquid-sintered tungsten–base alloys are a particle composite consisting of

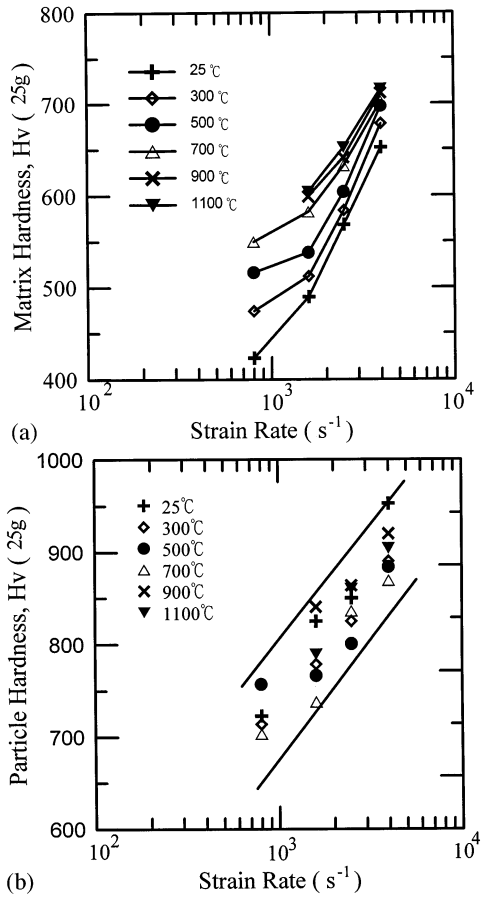

Fig. 12. Variations of microhardness as a function of strain rate and temperature in (a) matrix and (b) tungsten grains.

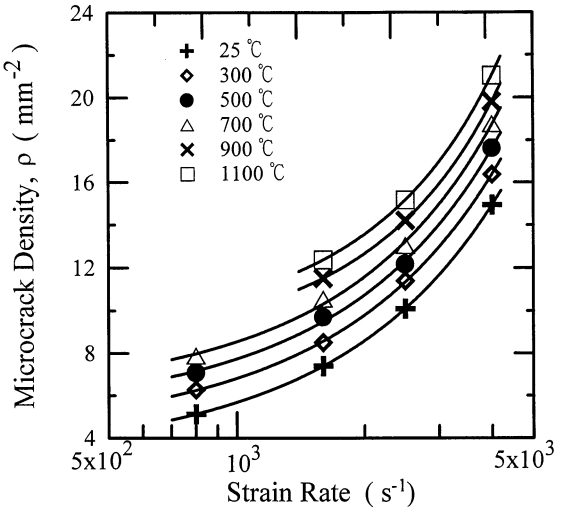

Fig. 13. Effect of strain rate and temperature on microcrack density of W–Ni–Fe composite.

rounded tungsten grains in a binder phase of nickel–iron solid solution, the stress configuration around the tungsten grains is very complex. The stress configuration depends on the tungsten grain volume fraction, the matrix composition and the flow strength of the tungsten phase. The flow strength of the tungsten phase depends on temperature, deformation rate and tungsten

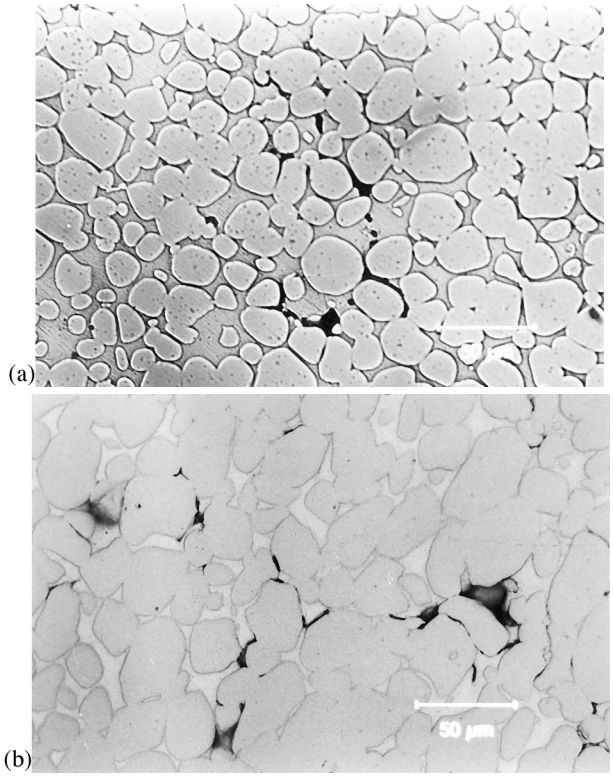

Fig. 14. Microcrack features obtained from specimens deformed at (a) 25°C with strain rate of 4×10^3 s^{-1} and (b) 1100°C with strain rate of 2.5×10^3 s^{-1}.

purity. Thus, during deformation, as critical fracture stress is reached, microcracks nucleate firstly at the interface of grain and matrix as well as at the grain–grain boundaries, because the resistance along an interface or a boundary is weaker than through the matrix or grain body. With increasing loading stress, initiated microcracks began to propagate with a mixture crack path, as described in the section on fracture feature observations, according to the local loading/material conditions. It must be noted, however, that even under conditions of heavy deformation, separation along the grain–matrix interface and grain–grain boundaries remains the major modes of failure. Exposed interface as opposed to transgranular cleavage sites constitutes the major characteristic of catastrophic fracture in our samples.

4. Conclusions

The deformation characteristics of W–Ni–Fe alloy by impact loading have been determined over a practical range of temperatures and strain rates. The results can be summarized as follows:

(1) The experimental results have demonstrated quantitatively that the major factors contributing to the strength of our tungsten composite during dynamic compressive deformation are the strain rate and temperature. The flow stress of the W–Ni–Fe composite increases with the strain rate, but an increase in the test temperature has an opposite effect. Moreover, work hardening decreases considerably as both the testing temperature and strain rate increase.

(2) For all testing temperatures, the linear dependence of flow stress on the logarithm of strain rate suggests that the deformation behaviour of W–Ni–Fe composite is dominated by the thermal activation mechanism. For an increase in temperature, strain rate sensitivity is found to increase. However, a decrease in strain rate sensitivity is observed when the temperature goes above 700°C. Temperature sensitivity also depends strongly on strain rate and temperature, and is slightly influenced by true strain.

(3) Based on our experimental results, a deformation constitutive equation incorporating strain rate and temperature effects is proposed to describe the observed flow stress–strain behaviour. By using our experimentally determined five parameters in our proposed constitutive equation, excellent agreement between the predicted data and the experimental measurement is found.

(4) Fracture surface observations indicate that our tungsten composite fails by a mixed fracture mode involving intergranular tungsten fractures, interfacial matrix–tungsten decohesion, tungsten cleavage and ductile rupture of the matrix. Microstructure observations reveal that microcrack density and grain deformation increase with strain rate and temperature until catastrophic crack propagation occurs. Initial microcracks nucleate preferentially at tungsten grain boundaries and tungsten–matrix interface. A strong dependence of microhardeness on strain rate and temperature is also found.

References

[1] S.W.H. Yih, Ch.T. Wang, Tungsten: Sources, Metallurgy, Properties and Applications, Plenum Press, New York, 1979.
[2] R.W. Penrice, Metals Handbook, 9th ed., vol. 7, American Society for Metals, Metals Park, OH, 1984, pp. 688–696.
[3] R.M. German, K.S. Churn, Metall. Trans. 15A (1984) 747–754.
[4] C.H. Lin, J.H. Jean, J. Mater. Sci. Lett. 2 (1983) 480–484.
[5] W.G. Northcutt, D.H. Johnson, F.E. Ferguson, W.B. Synder, Proceedings of the High Density Alloy Penetrator Materials Conference, AMMRC SP77-3, Army Materials and Mechanics Research Center, April 1977, pp. 25–36.
[6] D. Rittel, I. Roman, Mater. Sci. Eng. 82 (1986) 93–99.
[7] W.E. Gurwell, Annual Powder Metallurgy Conference and Exhibition, Boston, MA, Metal Industries Federation, May 1986, pp. 1–15.
[8] J.B. Posthil, M.C. Hogwood, D.V. Edmonds, Powder Metall. 29 (1986) 45–51.
[9] K.S. Churn, R.M. German, Metall. Trans. 15A (1984) 331–338.
[10] R.H. Krock, L.A. Shepard, Trans. AIME 227 (1963) 1127–1134.
[11] F.W. O'Neil, P.W. Salyer, Effect of tungsten composition on the mechanical properties of the W–Ni–Fe heavy alloy. AFOSR 66-1670, ASRL 132-2 USAF, MIT, Boston, 1965.
[12] H. Fischmeister et al. Plastic deformation of two phase materials with course microstructure, in: 3rd International Conference Strength Metals Alloys, Cambridge, 1973, pp. 621–625.
[13] D.G. Brandon, E. Ariel, J. Barta, Micromechanism of fracture in a W–0.5%Fe–0.5%Ni power composite, in: Proceedings 5th International Symposium, Electron Microscopy, Berkeley, CA, 1971, pp. 849–858.
[14] D.T. Eash, E.G. Zukas, W.V. Green, Report LA-4981-MS, Sci. Lab., University of California, Los Alamos.
[15] R.L. Woodward, N.J. Baldwin, B.J. Baxter, Metall. Trans. 16A (1985) 2031–2037.
[16] W.S. Lee, S.T. Chiou, Composites 27B (1996) 193–200.
[17] W.E. Gurwell, A review of embrittlement mechanisms in tungsten heavy alloys. Report PNL-SA-13646, Pacific Northwest Laboratory, Richland, WA, April 1986.
[18] L. Ekbom, in: H.H. Hausner, H.W. Antes, G.D. Smith (Eds.), Modern Developments in Powder Metallurgy, vol. 14, Metal Power Industries Federation, Princeton, NJ, 1981, pp. 177–188.
[19] R.H. Krock, L.A. Shepard, Trans. AIME 227 (1963) 1127–1134.
[20] R.G. O'Donell, R.L. Woodward, Metall. Trans. 21A (1990) 744–748.
[21] R.M. German, J.E. Hanafee, S.L. Digniallonardo, Metall. Trans. 15A (1984) 121–128.
[22] W.S. Lee, C.F. Lin, Mater. Sci. Eng. A241 (1998) 48–59.
[23] T. Nicholas, Exp. Mech. 11 (1971) 370–374.
[24] J. Harding, J. Mechanical behaviour at high rates of strain, in impact loading and dynamic behaviour of materials, in: C.Y. Chiem, H.D. Kunze, L.W. Megers (Eds.), DGM Informations Gesellschaft, Oberursel, 1988, pp. 23–42.
[25] W.S. Lee, H.F. Lam, J. Mater. Process. Technol. 57 (1996) 233–240.
[26] M. Zhou, A. Needleman, R.J. Clifton, J. Mech. Phys. Solids 42 (3) (1994) 423–458.

[27] F.J. Zerilli, R.W. Armstrong, Constitutive equation for hcp metals and high strength alloy steels, AD-vol. 48, High strain rate effects on polymer, metal and ceramic matrix composites and other advanced materials, ASME, 1995.
[28] G.R. Johnson, W.H. Cook, A constitutive model and data for metals subjected to large strains, high strain rates and high temperatures. Proceedings 7th International Symposium on Ballistics, The Hague, The Netherlands, April 1983.
[29] F.J. Zerilli, R.W. Armstrong, J. Appl. Phys. 61 (5) (1987) 1816–1925.